Metallography, Microstructure, and Analysis
volume 11, pages 309–326 (2022)
https://doi.org/10.1007/s13632-022-00846-x

$(FeMnNi)_{84}(AlTi)_{16}$ High-Entropy Alloy: Correlation of Microstructure, Strengthening Mechanisms and Hardness at Various Conditions (As-Cast, Solution Treated, Aged)

K. Konakoglou [1,2] · C. Mathiou [1] · E. Georgatis [1] · K. Georgarakis [2] · A. E. Karantzalis [1]

[1] Department of Materials Science and Engineering, University of Ioannina, Ioannina, Greece
[2] Sustainable Manufacturing Systems Centre, Cranfield University, Cranfield, UK

Abstract
A $(FeMnNi)_{84}(AlTi)_{16}$ high-entropy alloy was produced by vacuum arc melting successfully. The microstructure of the as-cast state showed the existence of two FCC phases along with potential precipitates. The solution treatment response of the alloy for 2 h at 1150 °C and the effect of aging time at 750 °C in the microstructure and microhardness were also evaluated. It was observed that the solution treatment parameters were insufficiently low to dissolve the as-cast precipitates into the matrix. The double FCC matrix identified may be correlated with a solidification range and insufficient diffusion during the solidification process. The maximum hardness at 90 min aging time can be mainly attributed to the precipitation shearing mechanism in both matrix areas. The lower hardness value reported at 160 h aging time was estimated that it is derived by the change of the main strengthening mechanism from shearing to Orowan. The island-like precipitates that depleted Ti element from the Ni-rich intergranular area may be identified as a Ni_2AlTi Heusler phase.

Keywords High-entropy superalloys · Solidification · Heusler phases · Strengthening mechanisms

Introduction

High-entropy alloys (HEAs) were introduced as bulk multicomponent equiatomic single-phase solid solution alloys that were firstly reported in 2004 by two separate studies from Cantor and Yeh et al. [1, 2] Within the following years, preliminary studies from various researchers illustrated promising mechanical properties, mainly as possible structural materials. It can be claimed that they "accidentally" derived from bulk metallic glasses (BMGs), in an attempt to clarify the possible impact of the increased configurational entropy that may lead to a higher glass forming ability [3].

HEAs' major difference compared to the conventional metallic alloys is changing the design goal. That is having five or more elements combined together with no dominant element, against the conventional way of having one main element acting as a matrix additively with small compositional quantities of other elements to provide the desired properties [3–5]. Additionally, HEAs offer some unique aspects; the cocktail effect, the "controversial" significant effect of lattice distortion [6], the sluggish diffusion effect and the mixing entropy, providing different design routes that can overcome some of the traditional metallurgical tradeoffs (e.g., strength–ductility ratio) [7, 8] and provide new materials with superior properties that none of the already optimized conventional alloys can currently achieve.

Nonetheless, as their research interest exponentially grew [9], their initial design goal and nature have been significantly changed. In the recent years, the researchers started to get advantage of the high configurational entropy, free energy and phase selection concepts with the sole goal to achieve the desired properties rather than strictly following the initial given definition(s). As expected, this aspect gradually broadens the field to purposely include alloys like non-equiatomic alloys, precipitation dispersed alloys [10], multiphase alloys [11, 12], medium entropy alloys (MEAs) [13, 14], functional materials [15–19] and films/coatings and fibers [20–22].

The conventional superalloys designed with the single element principle seem to reach their properties utilization

Published by Springer. This is the Author Accepted Manuscript.
The final published version (version of record) is available online at DOI:10.1007/s13632-022-00846-x. Please refer to any applicable publisher terms of use.

limits [23, 24]. Recently, a new HEA subfield emerged with possible attractive high-temperature properties, usually defined as high-entropy superalloys (HESAs) [10]. They mainly consist of a γ multicomponent equiatomic FCC HEA matrix to maximize configurational entropy and utilize HEAs' unique effects, strengthened usually with γ′ intermetallic and ideally intergranular precipitation [25–47]. Al and Ti elements are usually picked as γ' stabilizers for the desirable $L1_2$ and B2 phases [48] which are suitable for high-temperature structural applications, versus their usually undesirable brittle σ, Laves or grain boundary $L2_1$ counterpart phases [49, 50]. Additionally, the relatively low density of those elements is also one considerable advantage in the state-of-the-art fields like the aerospace industry.

HESAs' bigger compositional range allowing access to new compositions. Factors such as a) the low stacking fault energy, b) the positive lattice misfit between the FCC matrix and γ' precipitate, c) the high volume fraction and antiphase boundary (APB) energy of the $L1_2$ precipitate and d) the thermally stable microstructure are usually reported as the explanation for the properties' superiority over the conventional superalloys [25]. For example, HESAs' usual positive lattice misfit may attribute to more beneficial properties, versus the negative lattice misfit, which is usually found in the conventional Ni-superalloys [23, 51].

Despite their preliminary promising aspects, there are some crucial implications that need to be addressed. That is, the relatively low $L1_2$ solvus temperature (e.g., in FeCoCrNi matrix [40]) and the stabilization of the most favorable inter-granular $L1_2$ over the undesired σ, Laves and grain boundary $L2_1$ phases. Also, the effect of the precipitate nature, distribution, size, density and number relatively to the possible thermomechanical treatments needs to be extensively studied accompanied with much needed high-temperature assessments.

In the present work, the non-equiatomic $(FeMnNi)_{84(AlTi)16}$ HEA was prepared and studied to test its viability as a candidate element when designing the FCC matrix for FCC + $L1_2$ HESA microstructures. Manganese was selected as a possible cheaper option than the usually most reported Fe, Ni, Co, Cr, Cu elements in the literature [52]. Furthermore, manganese can contribute an even bigger atomic radii difference when added to the aforementioned elements, further enhancing the severe lattice distortion effect in the FCC HEA matrix [53]. Additionally, subsequent heat treatments were conducted to study the presence of Ostwald ripening on the precipitation that was tested via microhardness, XRD, SEM and EDS measurements. To the author's knowledge, there is limited work on manganese included FCC HESA matrix in the current literature, and as such, the present effort aims to enlighten further the behavior of this types of systems.

Experimental Procedure

Phase Formation Criteria

During the last years, many different parametric models have been developed in an effort to create useful tools in order to predict the possible phases that would form when designing a new high-entropy alloy system. Among these models, some gained significant attention and used extensively especially in the initial designing stages.

Zhang et al. [54], for instance, proposed the formation of solid solution phases to be related with three parameters: enthalpy of mixing (ΔH_{mix}) and entropy of mixing (ΔS_{mix}) for the involved elements and differences in the atomic sizes. These three parameters are given by the following expressions:

$$\Delta H_{\text{mix}} = \sum_{i=1, i\#j}^{n} \Omega_{ij} c_i c_j \qquad (1)$$

where $\Omega_{ij} = 4\,\Delta H_{mix}^{AB}$, ΔH_{mix}^{AB} is the mixing enthalpy of binary liquid AB alloys

$$\Delta S_{\text{mix}} = -R \sum_{i=1}^{n} c_i \ln c_i \qquad (2)$$

where R is the gas constant

$$\delta = 100 \sqrt{\sum_{i=1}^{n} c_i \left(1 - r_i/\bar{r}\right)^2} \qquad (3)$$

where $\bar{r} = \sum_{i=1}^{n} c_i r_i$, c_i and r_i are the atomic percentage and atomic radius of the ith element. The numerical factor 100 is used for simplicity reason. Based on this model, for a single solid solution phase to be formed, $-22 \le \Delta H_{mix} \le 7$ kJ/mol, $\delta \le 8.5$, and $11 \le \Delta S_{mix} \le 19.5$ J/(K·mol) have to be satisfied simultaneously.

Additionally, Wang et al. [55] focused on the effect the atomic size differences may have on the stability of single phases and introduced the geometric factor γ which is practically calculated based on the smaller and the larger of the involved elements:

$$\gamma = \left(1 - \sqrt{\frac{(r_s + \bar{r})^2 - \bar{r}^2}{(r_s + \bar{r})^2}}\right) \Big/ \left(1 - \sqrt{\frac{(r_L + \bar{r})^2 - \bar{r}^2}{(r_L + \bar{r})^2}}\right) \quad (4)$$

where r_s and r_L are the atomic radii for the smallest and largest atom and $\bar{r}$ is given by

$$\bar{r} = \sum_i^n c_i \cdot r_i \quad (5)$$

For a single phase to be formed, γ<1.175 must be established.

Troparevsky et al. [56] examined the enthalpies of formation of all the possible binary systems that could be formed for a given high-entropy alloy systems and they concluded that if the conditions where $137<\Delta H_f< 37$ meV/mol regarding a 5-component alloy (and $-232<\Delta H_f<37$ meV/mol for the refractory systems) are met, then a single phase should form.

Furthermore, the ci) factor, with ci) = $\Delta G_{ss}/-|\Delta G_{max}|$, adopted by King et al. [57], incorporates the thermodynamic factor ΔG_{ss} that is the change in Gibbs free energy for the formation of a fully disordered solid solution from a mixture of its individual elements and $_{\Delta Gmax}$ factor which is the lowest (intermetallic) or highest (segregated) possible Gibbs free energy obtainable from the formation of binary systems from the constituents of the mixture. According to this model, a value of ci) ≥ 1 suggests a stable solid solution at the systems' melting temperature and a negative ci) value recommends that the solid solution has positive formation enthalpy and will not form.

Guo et al. [58] introduced the concept of valence electron concentration (VEC) and the effect that it has on the stability of either BCC or FCC phases. They proposed that a value below 6.87 stabilizes the BCC structure and a value above 8 stabilizes the FCC one, with a mixed BCC and FCC structure being expected when VEC lies between 6 and 8. In another effort of them [59], they also took into consideration ΔH_{mix} and δ values and they suggested that a single solid solution is stabilized when $\delta \leq 6.6\%$ and $-1.6 \leq \Delta H_{mix} \leq 3.2$ kJ/mol, respectively.

Yang and Zhang [60] proposed a new thermodynamic parameter Ω, with:

$$\Omega = T_m \Delta S_{mix} / |\Delta H_{mix}| \quad (6)$$

where T_m is the melting point given by the mixture rule They suggested that a HEA with $\Omega \geq 1.1$ and $\delta \leq 6.6\%$ should be a simple solid solution.

Senkov et al. [61] introduced a theromydynamic model that predicts the presence or absence of intermetallic phases at given annealing temperatures T_A. This criterion is based on the relation between parameters such as $k_1^{cr}(T_A)$ and $\Delta H_{IM}/\Delta H_{mix}$. More specifically:

$$k_1^{cr}(T_A) = (1 - k_2) \cdot T \cdot \Delta S_{mix} / \Delta H_{mix} \quad (7)$$

$$k_2 = \Delta S_{IM} / \Delta S_{mix} \quad (8)$$

with ΔH_{IM} the enthalpy of formation of intermetallic phases, ΔH_{mix} the enthalpy of formation of solid solution, ΔS_{IM} the entropy of intermetallic phases and $_{\Delta Smix}$ the entropy of solid solution. According to these researchers, when values of $k_1^{cr}(T_A)$ are plotted versus those of $\Delta H_{IM}/\Delta H_{mix}$, clear separation of solid solution alloys from intermetallic containing alloys can be reported.

Jin et al. [62] criterion that focuses in the design of pseudobinary eutectic HEAs composed of FCC/B2 phases with the use of VEC and $_{\Delta Hmix}$ was also calculated for the present composition [62] More specifically, the parameters that are needed to be met are: (i) $VEC_{ss} \geq 8$ and $-5\ kJ/mol < \Delta H_{ssmix} < 0$, where VEC_{ss} is the valence electron concentration for the constituent elements of the FCC matrix, (ii) the melting temperature to room-temperature stability of the chosen intermetallic compound, (iii) the lowest enthalpy ΔH_f value among the arbitrary binary combinations in the alloy, for the dispersed intermetallic compound.

In general, the ΔH_{mix} and δ factors are widely accepted and used in the HEA's community as a useful empirical rule to predict the phase selection among solid solutions, inter-metallic compounds and the amorphous phase [63].

Materials and Methods

$(FeMnNi)_{84(AlTi)16}$ high-entropy alloy with a density of 7.64 g/cm^3 (rule of mixtures and experimental composition used) was produced by arc melting. The constituent elements, in the form of powders or wires, were of more than 99.5% purity and mixed. Melting was performed within a water-cooled Cu mold under argon protective atmosphere. Five remelting steps were performed in order to establish uniform elements/distribution within the final microstructure.

Specimens were prepared and subjected to solution treatment (ST, 1150 °C for 2 h), aging (750 °C for 30–9600 min, respectively).

An X-ray diffractometer (Bruker, D8 Advance) using a scanning rate of 0.01°/s was used for the assessment of the crystal structure which was further analyzed with the use of Match!3 software. Two scanning electron microscopes (TESCAN S8000G and JEOL 6510 LV) equipped with both backscatter electron (BSE) and energy-dispersive spectroscopy (EDS) detectors (Oxford System) were used in order to examine the microstructure. Standard metallographic procedure and chemical etching with diluted Aqua Regia solution (200 mL Ethanol, 75 mL HNO_3, 25 mL HCL) for a duration of 1 were adopted for each SEM sample. Vickers microhard-ness HV1 was measured on polished surfaces under 1000 g load applied for 10 s.

The fraction, surface area and mean diameter of the precipitates were measured by the use of Image J software. This procedure involves the conversion of 225 gray-level BSE images into black (precipitates) and white (FCC matrix) binary images.

Basic thermodynamic calculations were performed using FactStage version 8.1.

Table 1: Nominal and actual composition of the as-cast (A.C.) alloy.

		Atomic percentage at%				
		Fe	Mn	Ni	Al	Ti
(FeMnNi)84(AlTi)16 as-cast	Nominal	28	28	28	8	8
	Actual	30.75	22.39	30.18	7.74	8.95

Table 2: Phase criteria, thermodynamic factors values and the experimental composition values for the as-cast investigated alloy

		δ	ΔS_{mix} (J/mol·K)	ΔH_{mix} (kJ/mol)	VEC	Ω	γ	Φ	$\frac{\Delta H_{IM}}{\Delta H_{mix}}$	k_{cr}^1
(FeMnNi)84(AlTi)16 as-cast	Nominal	5.81	12.48	-20.59	8.30	1.15	1.183	0.26	1.41	1.20
	Actual	5.96	12.24	-17.49	8.44	1.03	1.195	0.26	1.73	1.23

meV/atom	Al	Ti	Fe	Ni	Mn
Al	0	-428	-369	-677	-278
Ti	-428	0	-418	-435	-277
Fe	-369	-418	0	-97	9
Ni	-677	-435	-97	0	-115
Mn	-278	-277	9	-115	0

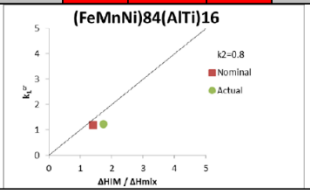

Table 3: Jin's [62] numerical criteria calculation for the present (a) theoretical and (b) experimental composition of the A.C. alloy.

(a)	VECss	$\Delta H_{\text{mix}}^{ss}$	(b)	VECss	$\Delta H_{\text{mix}}^{ss}$
	8.3	−4.4 kJ/mol		**8.47**	−4.26 kJ/mol

Table 4: The atomic radii of the Fe, Mn, Ni, Al and Ti elements

Element	Atomic Radius (Å)
Al	1.432
Ti	1.462
Fe	1.241
Mn	1.350
Ni	1.246

Results

Phase Formation Criteria

The experimental and theoretical values of the as-cast alloy were used to calculate 7 different phase criteria for HEAs (Table 1). Two of them suggested the formation of a simple solid solution [60, 62] while four of them anticipated phase segregation or formation of intermetallic phases [55–57, 61]. The exact criteria values for the investigated composition, both theoretically and experimentally are listed in Table 2. The valence electron concentration (VEC) as proposed by Guo [59] was calculated equal with 7.56 predicting a mixed FCC+BCC structure.

Especially in the case of the Jin's model [62], the calculated values for the current composition are illustrated in Table 3. The AlTi intermetallic compound has the highest melting point (~1450 °C) against the second-best candidate TiNi (~1300 °C) [64, 65] Moreover, AlTi exhibits the lowest $\Delta H_{mix} = -61\ kJ/mol$ compared against the runner up AlNi, (AlNi $\Delta H_{mix} = -49\ kJ/mol$) (Miedema Calculator) [66–68].

The Fe, Mn, Ni elements are expected to act like a FCC matrix for the AlTi dispersed phase, as suggested by the aforementioned criteria. Additionally, Al and Ti elements have the largest atomic radii in comparison with Mn, Fe and Ni, supposedly providing more tendency for segregation via particle/matrix mismatch in the FeMnNiAlTi system (Table 4, the atomic radii were taken from [59]). Besides, the ΔH_f of the binary compounds between manganese, iron and nickel were included in the boundaries that Troparevsky's criterion suggested [56]. Lastly, the simultaneous and uniform fluctuation of the aluminum and titanium elements between the Fe-rich and Ni-rich area (this separation will be explained later) suggests that compounds including the two elements, act together as a solute phase in the FCC FeMnNi matrix.

XRD Patterns Interpretation

Out of a total 12 XRD patterns (Figs. 1 and 2), the strongest peaks at 43, 50, 73.5° 2 theta can be mainly correlated to a double FCC matrix. The double peaks near 43° may be attributed to the difference in Fe at% content between the two areas, leading to slightly shifted peaks due to the change in lattice constants [69]. Moreover another factor that may induce the separation of the two peaks is the difference in the solute Ti at% between the two areas, since it is recently reported that it can lead to this phenomenon [70]. The last statement about Ti at% content might be considered as a major mechanism that eventually merged the double FCC matrices' peaks after a critical aging point, since the possible Heusler particles can impact the Ti content in Ni-rich areas, as it will be discussed in detail further below in the text. The average lattice constant calculated for the matrix in this experiment was 0.3599 nm, which is close to Zhang's et al. work of 0.3607 nm for the $Fe_{50.40}Mn_{25.62}Ni_{23.98}$ at% [69].

The Heusler Ni_2TiAl with a $L2_1$ structure that was matched can be originated from a supersaturated B2-TiNi matrix [71]. Both ordered structures are based on BCC structure. Also, the complicated nature of the diffraction pattern of this system may add up extra difficulty into the identification and interpretation, with a possible total of three different types of peaks, A2 lattice and $L2_1$ and B2 superlattices, as reported in a powder diffraction spectrum for a Ni_2AlTi compound [72]. That might be the reason that in FCC matrix AlTi dispersed HEAs, peaks that correspond to precipitated compounds are usually identified as either Heusler, B2 or $L2_1$ in XRDs or equivalent methods. [37, 40, 41, 70, 73, 74]. For the readers' assistance, Figure 3 is a 2 theta versus heat treatment graph of the 2 peaks included in the rectangle shadow regions in the aforementioned XRD patterns, showing their alteration with heat treatment.

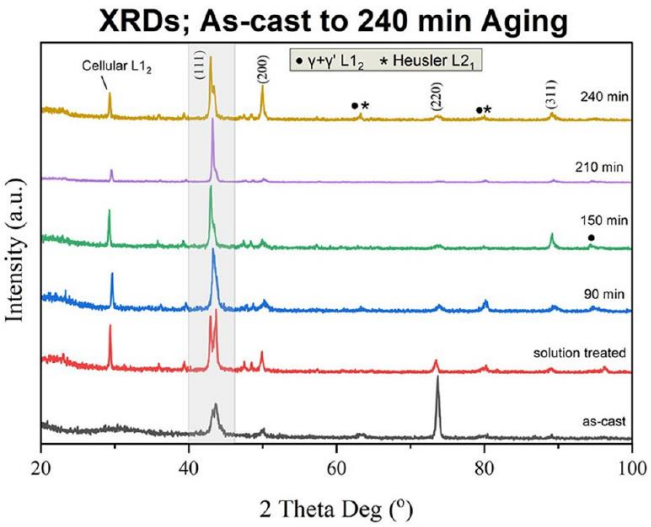

Figure 1: The 12 XRD patterns for the as-cast, solution-treated, aged for 90, 150, 210 and 240 min specimens. The symbols at 240 min pattern identify the phase present in each peak. The gray color highlights the 43° peaks that were discussed in detail

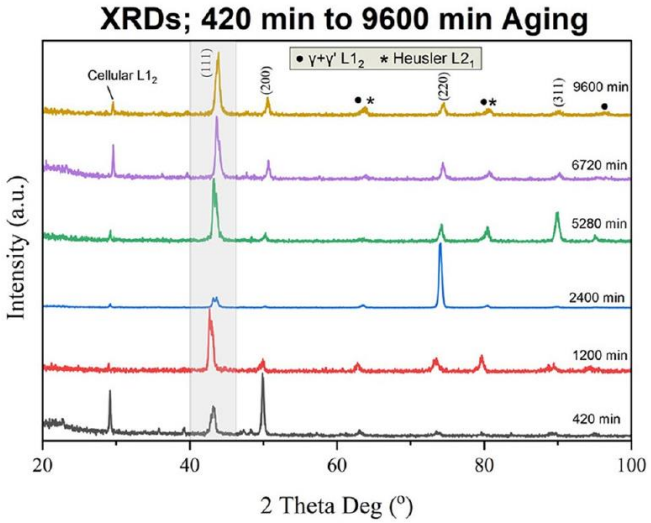

Figure 2: The 6 XRD patterns for the 420, 1200, 2400, 5280, 6720 and 9600 min aged specimens. The symbols at 240 min pattern identify the phase present in each peak. The gray color highlights the 43° peaks that were discussed in detail.

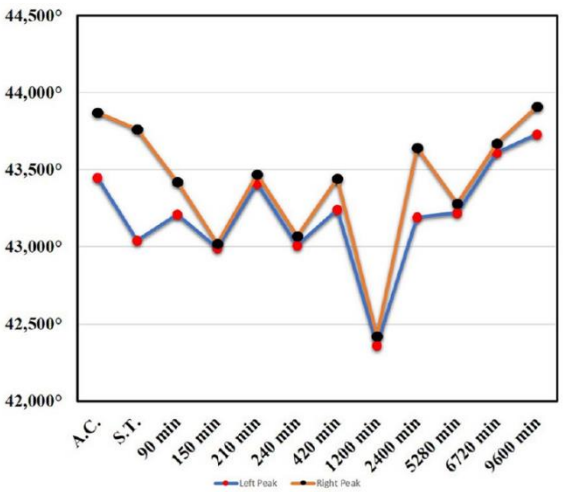

Figure 3: 2 theta versus thermal treatment graph of the 2 peaks included in the rectangle shadow regions in Figs. 1 and 2

As-cast and Solution-Treated Microstructural Observations

The as-cast (A.C.) specimen microstructure after SEM inspection at different magnifications is shown in Fig. 4. Two distinct phases can be observed: a bright phase of characteristic dendritic morphology and a dark phase associated with the interdendritic region. Further examination with EDS mapping, Fig. 5a, reveals that the bright phase is enriched in Fe and the interdendritic phase in Ni, respectively. EDS line scanning, Fig. 5b, also verifies the same tendency.

A similar situation is observed in the case of the solution-treated (S.T.) specimen. Fig. 6 presents its microstructure after SEM examination at different magnifications and Fig. 7 a and b shows the EDS chemical mapping and line scanning analysis, respectively. The only distinguishing difference is the extinction of the dendritic structure, with the involved bright and dark phases possessing more rounded morphologies. Apart from this, their compositional profiles do not seem to be altered compared to the A.C. state.

These microstructural observations come to support and verify the XRD results about the existence of a double FCC phase. Furthermore, this double FCC presence has been systematically described by Zhang et al. [69]. These researchers studied the new phase transitions temperatures and phase equilibria and schemed a FeMnNi ternary phase diagram. The calculated vertical section of this ternary phase diagram at 30 wt.% Mn seems to fit relatively close with the converted experimental weight percentages of the current experimental procedure (A.C.: $_{Fe0.55Mn0.45}$ ^{and} Ni0.57Mn0.43 wt.%, versus $_{Fe0.70Mn0.30}$ ^{and} $_{Ni0.70Mn0.30}$ wt.% of the discussed vertical section), and it was used as reference point. The specific diagram was mainly used due to its compatibility in terms of the same compositional content of Mn in both areas. The modified diagram is at Fig. 8. The perpendicular black line highlights the approximately experimental composition of the A.C. alloy, which is close to 1/1 ratio (Fe: 38.23 wt.%, Ni:40.66 wt.%).

Therefore, based on the XRD analysis, the SEM – EDS examination and the postulates of Zhang et al. [69] work, a potential solidification sequence includes the formation of either $L1_2$ and/or Heusler ($L2_1$) precipitates as a first stage with the remaining liquid being solidified in a way approached by the following equation:

$$\begin{aligned} L &\rightarrow L' + \text{FeMnNi}(\mathbf{Fe-rich}) \\ &\rightarrow \text{FeMnNi}(\mathbf{Fe-rich}) + \text{FeMnNi}(\mathbf{Ni-rich}) \end{aligned} \quad (9)$$

Summarizing, the solidification range illustrated in Fig. 8 during the cooling process could be the main attributor of the microsegregation phenomenon in the microstructure. The first-to-solidify (the L´ factor of the equation) liquid melt that crossed the liquidus line solidified to a Fe-rich FeMnNi phase, relatively to the initial global composition of the primary liquid, whereas the secondary melt (the L' factor of the equation) that coexisted with the first-to-solidify Fe-rich FeMnNi solidified to a Ni-rich FeMnNi phase, again relatively to the primary liquid. The approximately high cooling rate of the current experiment hindered the diffusion that was supposed to take place and contributed to the enclosure of this microstructure until room temperature.

If the diffusion would happen without constraints, the final microstructure might be consisted of a FCC single solid solution, just like the original Fig. 8 diagram and phase criteria suggest.

Further support for the existence of the previously mentioned phases comes from the thermodynamic calculations performed by FactStage. Fig. 9 shows the phases predicted for the case of the actual composition (Table 1) of the prepared system. The calculations predict the stability of an FCC solid solution above roughly 950 °C. Interestingly, below 950 °C, the calculations predict the presence of additional phases such as Ni_3Ti and $L1_2$. Moreover, Fig. 10 shows the phase predictions for the pseudobinary FeMnNi – AlTi phase diagram which is a good approximation of the actual system prepared in the present effort. The black dash line represents the closer to the actual composition AlTi/ AlTi+FeMnNi molar ratio. Based on the predictions of this phase diagram, the system seems to contain: (a) a first solid FCC solid solution (FCC_1), (b) second FCC solid solution (FCC_2), (c) a L12 phase and (d) a Ni_3Ti phase. This observation refer to the temperature of 700 °C. Both Figs. 9 and 10 verify in general the XRD results. The only exemption, nevertheless, is the presence of Ni_3Ti phase which is not clearly identified by the XRD analysis. Its possible existence could be associated with the multiple small peaks around 46°, yet further experimentation is required. It should be, nevertheless, wise to include as another potential phase at the onset of solidification, that of the Ni_3Ti intermetallic.

Last but not least, it has to be mentioned that the same two FCC phase segregation scenario seems to persist also for the 160 h aged specimen. Tables 5 and 6 show the mean values of various EDS point analyses for the two segregated FCC phases in the three different specimens (A.C., S.T., 160 h aged). Clearly, the Fe and Ni segregated compositional profiles can be observed.

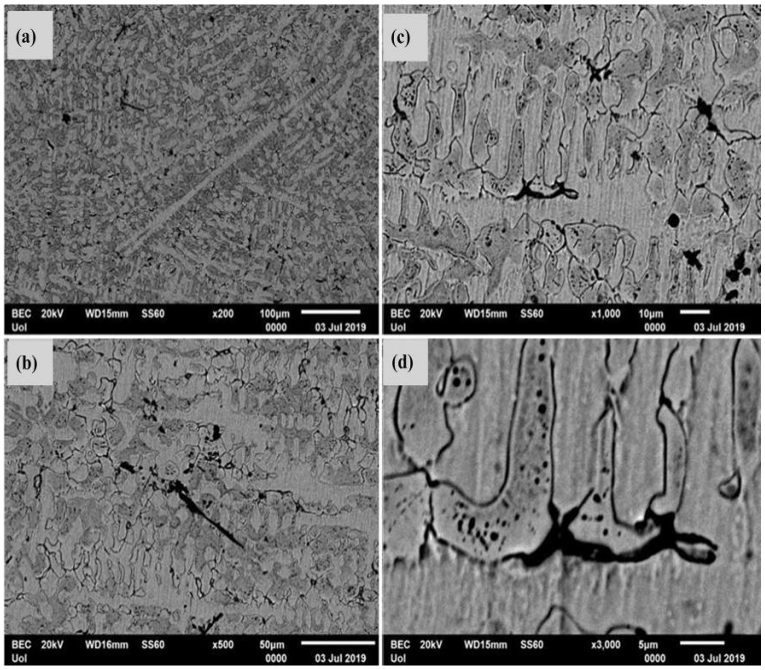

Figure 4: SEM images of the as-cast microstructure at different magnifications. It can be observed that two major phases are present: a light phase of characteristic dendritic morphology and a dark interdendritic phase.

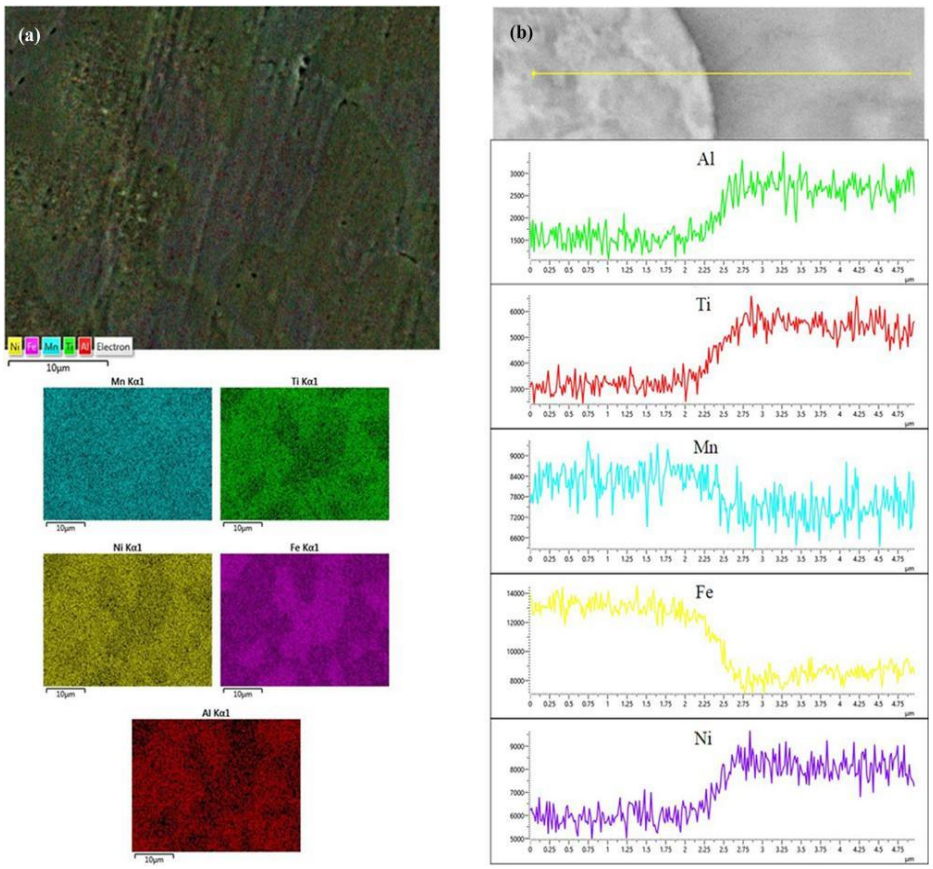

Figure 5: As-cast: (a) EDS mapping analysis showing segregation of elements in the two major phases, (b) EDS line scanning showing similar elemental segregation.

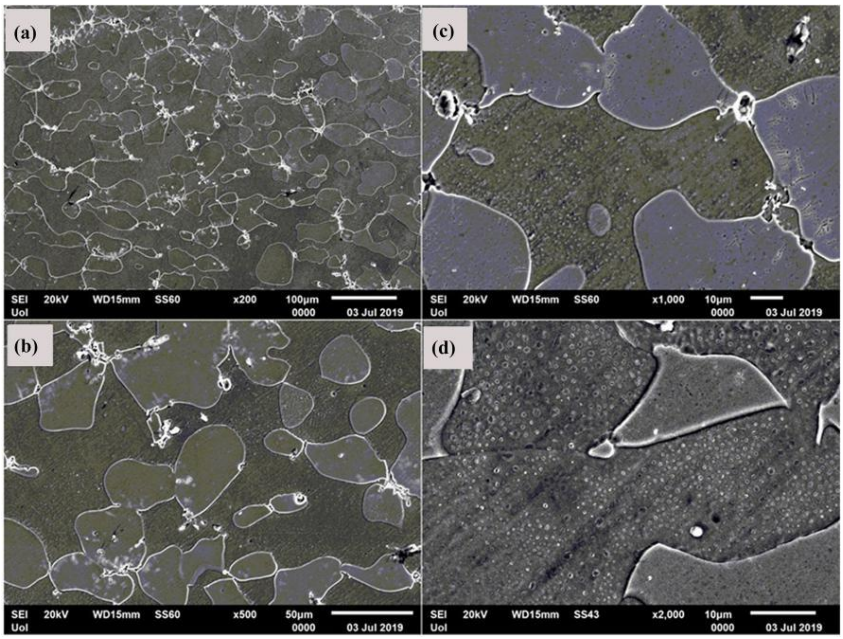

Figure 6: SEM images of the solution-treated specimen. It can be observed that the two phases formed at the as-cast state still persist, yet their morphology has been dramatically modified with the main feature being the elimination of the dendritic structure.

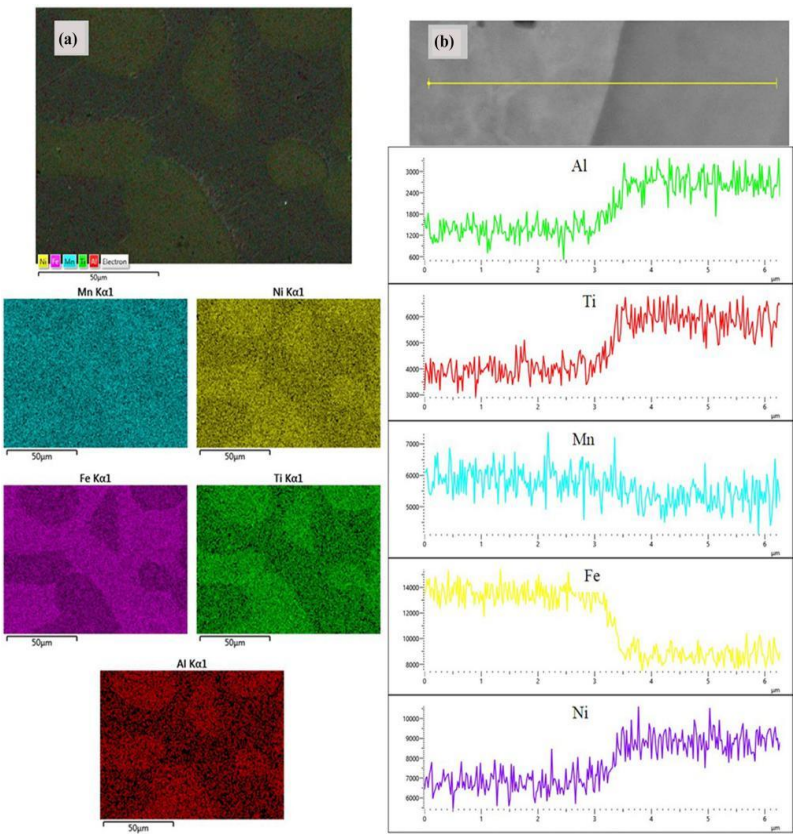

Figure 7: Solution treated: (a) EDS mapping analysis showing segregation of elements in the two major phases, (b) EDS line scanning showing similar elemental segregation

The Effect of Heat Treatments

Heat treatments can usually impact the microstructure of an alloy through mechanisms like the Ostwald ripening and Hall–Petch effects. Hence, it is believed that these phenomena can affect the mechanical properties of the systems produced in the present effort. Extensive room-temperature Vickers microhardness tests were conducted in all of 12 specimens for the evaluation of the possible strengthening mechanisms present in each alloy. Fig. 11 illustrates the influence of heat treatments to the mechanical properties, with all the reported values being relatively high for a soft single-phase FCC HEA [75–77]. The microhardness reaches its maximum value at 90 min of aging time (399 ± 20 HV1), while afterward it follows a mostly downward trend until 160 h aging time (300 ± 10 HV1). Interestingly, an unexpected decrement and increment, with regard to the typical age hardening behavior, occurred at the S.T. and the 1200 min treated specimen, respectively. Also, the two aforementioned specimens showcase the biggest variation in between their measurements (S.T.: 326 ± 31 HV1; 1200 min: 371 ± 33 HV1). The variations tend to get narrower from 2400 min and onwards. These trends will be further evaluated with regard to the intergranular nanoprecipitates below.

A preliminary statistical analysis was conducted in order to assess the particles' average diameter and diameter distribution, by using SEM images, in the A.C. and 160 h aged specimens. The diameter histograms for both areas in A.C. and 160 h aged specimen are shown in Fig. 12. The average diameter of the nanoparticles in A.C. was found to be 23.7 ± 10.6 nm and 20.3 ± 9.6 nm for Fe-rich and Ni-rich area, respectively, while the average diameter in 160 h aged specimen was found to be 59.8 ± 17.7 nm and 26.0 ± 6.0 nm for Fe-rich and Ni-rich areas, respectively. The calculated area fraction of the precipitates in Fe-rich area for 160 h specimen was found to be 34.81 ± 4.40 %. It can be observed that the combination of the heat treatments and the Fe-rich matrix led to a distinguishable coarsening of their corresponding nanoparticles, as Fig. 13 illustrates.

Hardness Interpretation Through Strengthening Mechanisms

It is established that the main factors that attribute to yield strength in polycrystalline materials are, lattice friction (o_i), solid solution strengthening (o_{ss}), grain boundary strengthening $_{(ogb)}$ and precipitation hardening (o_k) [78, 79]:

$$\sigma_y = \sigma_i + \sigma_{ss} + \sigma_{gb} + \sigma_p \qquad (10)$$

Additionally, yield strength usually illustrates a linear correlation with hardness in metals, like in the case of steels [80]. Unfortunately, the assessment of solid solution strengthening in HEAs is still a challenge, since it is no clear which are the solute and solvent atoms [41]. Moreover, since the alloys in this study have identical chemical composition, it was hypothesized that $_{is}$ and a_i are not the most influential factors in the following interpretations.

Through the comparison of the A.C. and S.T. microstructures in Figs. 4 and 6, it is visible that the grain boundaries got smoother after the solution treatment. The dendritic structure in A.C. is transformed into equiaxed grains in S.T. This microstructural alteration has a significant effect on the overall grain boundary extent. By comparing Fig. 4b,c and Fig. 6b,c, it can be observed that this alteration form den-dritic to equiaxed morphology also results in a considerable reduction of the overall grain boundary areas. The extensive dendritic contour spread out between the primary and the secondary dendritic branches is almost eliminated and substituted by a smooth almost circular contour of the equi-axed grans. This modification theoretically leads to the lower grain boundary strengthening that was observed through the microhardness measurements in Fig. 11. This may explain the slight drop in the average HV1 microhardness between A.C. and S.T. The grain boundary strengthening contribution can be qualitatively evaluated in the present case with the following equation:

$$\sigma_{gb} = K_y \times d^{-\frac{1}{2}} \qquad (11)$$

where K_y is Hall–Petch strengthening coefficient and d is the average grain size.

To further clarify the high deviation in the micro-hardness in the S.T. specimen, HV0.025 measurements were conducted. HV0.025 microhardness (10 s application of load) after chemical etching with Aqua Regia was performed in order to reveal the grain boundaries and solely evaluate Fe-rich and Ni-rich areas. Through the visual inspection of the indent's marks and microhard-ness measurements in both microstructures, the Ni-rich matrix appears to be significantly harder (Fe-rich: 556 ± 53 HV0.025, Ni-rich: 854 ± 29 HV0.025). The indents' marks can be observed in Fig. 14. This behavior can be attributed to a possible higher precipitates density in the Ni-rich area versus the Fe-rich. The higher compositional amounts of Al and Ti elements can be responsible for nucleating more intergranular precipitation providing increased strengthening (Tables 5, 6). Also, the increased load of the HV1 initial measurements might have increased the area of indent's mark on the sample, ending up measuring multiple Ni and Fe-rich areas, enhancing the fluctuation of final microhardness value.

Precipitation can lead to significant strengthening of an alloy, through the different sizes and morphologies that could be resulted as a function of time. Fundamentally, the aforementioned phenomenon can happen via either of the following well established mechanisms; (i) by dislocations that cut through the precipitates, (ii) or/and by dislocations that bypass the precipitates by a looping mechanism (Orowan), which interestingly are also reported in many HEAs [28, 35, 36, 41]. The occurrence of each mechanism is mainly governed via the diameter of the precipitates. Hence, particle shearing will dominate when the particle sizes are below d_c (usually between 5 and 50 nm), giving its place to Orowan when exceeding a critical value [81].

Leskovsek et al. [82] have adopted an empirical equation to estimate the average distance l between carbide particles in high-speed steels:

$$l = d \times (1 - f) \times \sqrt{\frac{2}{3 \cdot f}} \quad (12)$$

where f the precipitates' volume fraction and d the average diameter

The shearing stress for the precipitates (σsh) and Orowan stress (σOr) can be expressed as:

$$\sigma_{sh} = 0.81M\frac{\gamma_{APB}}{2b}\left(\frac{3\pi f}{8}\right)^{\frac{1}{2}} \quad (13)$$

$$\sigma_{Or} = \frac{Gb}{2\pi l} ln\left(\frac{l}{r_0}\right) \quad (14)$$

where M is the Taylor factor (3.06 for FCC alloys), γ_{APB} is the antiphase boundary (APB) energy of the $L1_2$ Ni_3Al (184 mJ/m^2), b is the Burgers vector (~ 0.262 nm), l is the average particles'distance, r_0 is the dislocation core radius ($r_0 \approx b$), and G is the shear modulus (78.5 GPa), as it was used by Peng et al. [28]. With the usage of the aforementioned data to approximate the present alloys, a theoretical-ideal shear-ing/Orowan stress versus diameter was schemed to estimate the critical transition diameter between the 2 ambivalent mechanisms (Fig. 15). The volume fraction used in Fig. 15 was 25% for 15 nm diameter and gets its maximum value at 36% for 60 nm, with linear increment. These values were picked to match the 160 h specimen diameter and area fraction in the current experiment and the f values reported in the literature [28, 30, 36, 41]. For the reader's more clear understanding, few more comments should be added concerning the interpretation of Fig. 15:

- The blue line shows the effect the particle size has on the strengthening effect accumulated by the particle shearing mechanism. According to this trend the higher the particle size, the more increased the strengthening result.
- The orange line shows the same effect of the particle diameter on the strengthening effect due to the Orowan strengthening mechanism. According to this, the higher the particle diameter the more faded the strengthening events.
- D critical $(d\text{critical})$ is the critical particle diameter at which both mechanisms can provide the same strengthening effect. Below $d\text{critical}$, strengthening by the Orowan mechanism is higher than that of the particle shearing mechanism. On the contrary above the $d\text{critical}$ the Orowan dislocation particle by passing mechanism is easier and as such its strengthening effect is reduced.
- Hardness interpretation at the different heat treatment stages is based on three different key factors: (a) the strengthening mechanism that is established, in case, as a function of the particle diameter (b) the different rate of the Fe-based and Ni-based particle coarsening behavior and (c) the rate of particle precipitation—and hence their fraction—especially in the case of the Ni- based precipitates.

As the histograms in Fig. 12 suggest, the precipitates in both areas possess about the same diameters, which translates into both areas get mainly strengthened with the shearing mechanism with regards to i_p (1st Mark). As the aging time increases, the precipitates get ripen with different rates with regards to the 2 different areas as well, but all of them contribute positively to the hardness. The highest hardness achieved at 90 min may be the critical point where the Fe-rich precipitates have reached their maximum mean strengthening (average diameter close to $d\text{critical}$). The Ni-rich ones are possibly still below the critical value, because even after 160 h of aging time, they still possess a mean diameter of 26.0 ± 6.0 nm, which is around the critical value. The decrement in the 3rd mark's area is due to the Orowan mechanism slowly overtaking the precipitates of the Fe-rich area, negatively affecting the hardness with a higher rate than the shearing mechanism of the precipitates in the Ni-rich area can increase it. The Ni-rich precipitates are still in the shearing strengthening area. The increment of the hardness in the 4th mark is where the Ni-rich area precipitates strengthening via shearing mechanism overrun the Orowan mechanism of their Fe-rich counterparts. This can be explained by both the broadened slope in the Orowan area, and the higher precipitate density of the Ni-rich area. The double amount of Al, Ti elements, possibly nucleated more precipitates and provided more strengthening than its Orowan strengthened counterpart. Lastly in the 5th mark, Ni-rich area precipitates' mean diameter approaching the $d\text{critical}$ value, and as a result, the summary alloys' hardness starts decreasing as aging time increases, as expected by a typical overaging behavior.

The Correlation Between Intergranular and Grain Boundary Precipitates

Tables 5 and 6 illustrate the corresponding Al/Ti at% ratios. With the present experimental data, it is evident that there is a mechanism that gradually depletes the Ti element from the intergranular Ni-rich area (A.C.: 0.44, 160 h: 0.74), where the same phenomenon seems to be absent in its Fe-rich counterpart (A.C.: 0.51, 160 h: 0.54).

Through inspection of Fig. 13a-c, a new phase along the grain boundaries, in between the Ni-rich and Fe-rich areas, can be observed, when comparing the A.C. and 160-h-aged microstructures. This phase has identical chemical composition with the Fe-rich area.

Murdoch [83] developed a model that predicts the tendency of elements to be segregated at the grain boundaries, based on Miedema-type approach. According to this model, in Ni-X type solid solutions, atoms such as Ti and Al exhibit a considerable tendency to be segregated at the grain boundaries, due to their high (positive) values of segregation enthalpy (ΔH_{seg}). Additionally, compared to Fe, Mn and Ni (elements with the similar atomic radius, about 1.241, 1.350 and 1.246 Å [58]), Ti and Al have larger atomic sizes (Ti = 1.462, Al = 1.432 Å [58]). This aspect can cause localized supersaturated areas that can establish high particle/matrix mismatch which, in turns, lead to increased strain energy of the surrounding FCC matrix promoting; thus, the formation of discontinuous cellular phases at the grain boundaries [33]. Cellular precipitates along the grain boundaries are commonly reported in similar FCC+$L1_2$ microstructures. [27, 32, 33, 38, 40].

Numerous researchers reported Heusler phases at the grain boundaries regarding AlTi dispersed HEAs [33,37,40,41,74)]. It is reported that the increased super-saturation of Ti and Al can thermodynamically destabilize the cellular $L1_2$ structure, a fact that favors the formation of locally stabilized ordered-BCC Heusler phase at the grain boundaries [33]. Choudhuri et al. [73], by using DFT calculations, also postulate that Ti is necessary to promote the stabilization $L2_1$ phase in the well-characterized B2-forming CoCrFeNiAl HEA. Their morphology is reported as large island-like precipitates near the grain boundaries, causing sags and crests due to the Zener pinning effect [27].

Figure 16 illustrates an EDS line scan for an island-like precipitate near the grain boundary, accompanied with a high-resolution SEM image. The distinct Ti element peak indicates the possible segregation of Ti element in the particle, while the SEM image shows its morphology. The thermodynamic data comparison that was found in the literature for the present Z element candidates in the Ni_2AlZ Heusler phase were the Fe, Mn, Ni, Al and Ti elements. The heat of formations of all the possible Ni_2AlZ phases is presented in Table 7 [65–67, 73, 84, 85]. The current data comprise another potential evidence of Heusler phase presence, since the lowest heat of formation is accounted for the Ni_2AlTi compound, proposing its stability over the ambivalent compounds. Additionally, the same compound appears to be detected in numerous of the aforementioned AlTi dispersed HEAs, as in the case of both He's et al. works where $L2_1$-Ni_2AlTi/$(Ni, Co)_2AlTi$ Heusler particles, are formed mainly along grain boundaries [40, 41]. In Zhao's et al. work as the same Ni_2AlTi compound [35], and lastly in Yang's et al. work, it is reported that the presence of excessive Ti additions will promote the formation of $L2_1$ particles of more brittle nature at grain boundaries (not mentioning Heusler characterization, just the same crystal structure and general morphology) [37]. The formation of the Heusler particles can explain the initial hypothesis of a possible Ti depletion mechanism for the Ni-rich FeMnNi area, suggesting a Ti segregation to these particles. The gradual Ti element depletion in the Ni-rich area may be the main mechanism that altered the precipitate mean diameter between the two areas.

The precipitation extent and morphology, especially in the case of the Ni-rich phase, can also be supported by means of pseudospinodal decomposition phenomena. Pseudospinodal decomposition is the case where when the alloy composition overpass a critical c_0 value, a congruent (partitionless) $a_2 \rightarrow y$ transformation is firstly established, followed by decomposition, also leading to high nucleation density [84–87]. This phenomenon within a narrow compositional range (e.g., $\Delta_c \approx 2\%$) can increase the particle number density by 3-4 orders of magnitude [80, 84]. The EDS data in Tables 5 and 6 showed approximately half the amount of Al, Ti elements in the Fe-rich area versus the Ni-rich area. With the use of the available experimental data, we can hypothesize that the microstructure behaves as like a pseudobinary system that consists of the FCC FeMnNi matrices, with the AlTi dispersed phase. The preferably depletion of Ti element in the Ni-rich area over the Fe-rich, gradually pushed the Al/ Ti at% ratio above the critical composition where the pseu-dospinodal decomposition phenomenon occurs. As the aging time increased, Ni-rich area secondarily nucleated exponentially more new particles that caused significantly more contest over the solutes Al, Ti among the intergranular precipitates, relatively to the Fe-rich area. Additionally, the increased initial compositional amount of Al, Ti elements in the Ni-rich area surely played a major role in initially nucleating more primary particles as well (Tables 5 and 6). The less amount of available solute Al, Ti led to slower coarsening rate of the Ni-rich precipitates over the Fe-rich ones, even though they initially nucleated within the same diameter range (Fig. 10). The explanation proposed here seems to align with both the experimental and literature data provided.

Conclusions

In this study, the solution treatment capability for 2 h at 1150 °C and the effect of aging time at 750 °C in the microstructure and microhardness was evaluated for the $(FeMnNi)_{84(AlTi)16}$ alloy. The following conclusions were extracted:

1. The solution treatment parameters of 2 h at 1150 °C were insufficiently low to dissolve the as-cast precipitates into the matrix, as visible precipitates were identified in both as-cast and solution treated samples. This suggests that the solvus temperature of the studied system lies above the temperature used in the present work.
2. The double FCC matrix identified may be correlated with a solidification range and insufficient diffusion during the solidification process.
3. The maximum 399 ± 20 HV1 at 90 min aging time can be mainly attributed to the precipitation shearing mechanism in both matrix areas. The 300 ± 10 HV1 reported at 160 h aging time was estimated that it is derived by the change of the main strengthening mechanism from shearing to Orowan.
4. The island-like precipitates that depleted Ti element from the Ni-rich intergranular area may be identified as a Ni_2AlTi Heusler phase, which further enhances the literature data that suggest its stabilization via the presence of Ti in HEAs.

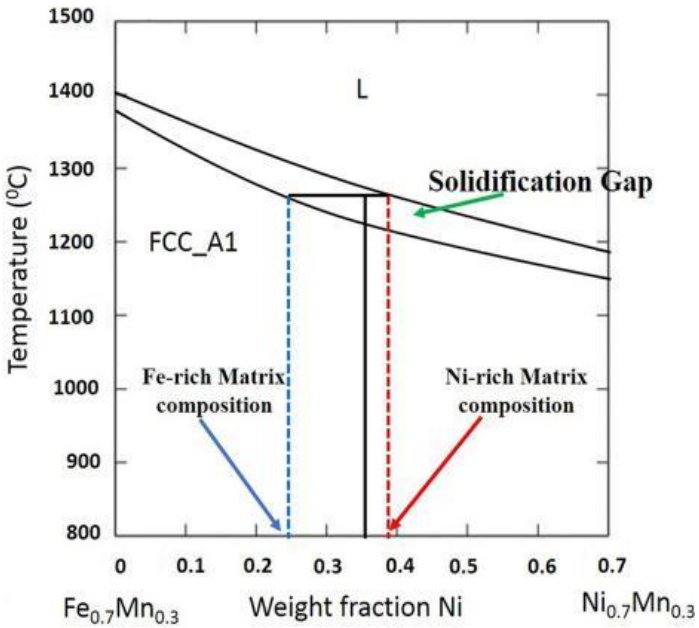

Figure: 8 The modified calculated vertical section at 30 wt.% Mn, as calculated by Zhang et al. and based on [69]. It demonstrates the weight fractions of $_{Fe0.7Mn0.3}$ (on the Left axis) and $_{Ni0.7Mn0.3}$ (on the right axis), for temperatures ranging from 1500 °C to 800 °C. The solid black line illustrates the theoretical area of solidification for the FeMnNi matrices. The dotted lines show how the final speculated compositions of Fe-rich and Ni-rich matrices might have been formed. The existence of the solidification gap may explains the segregation between the 2 areas.

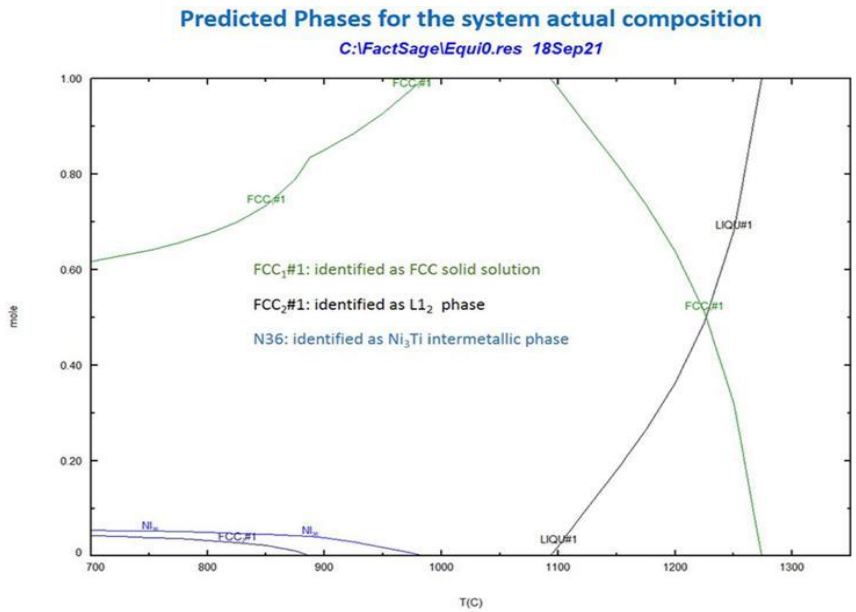

Figure 9 FactStage phase predictions for the actual composition of the system

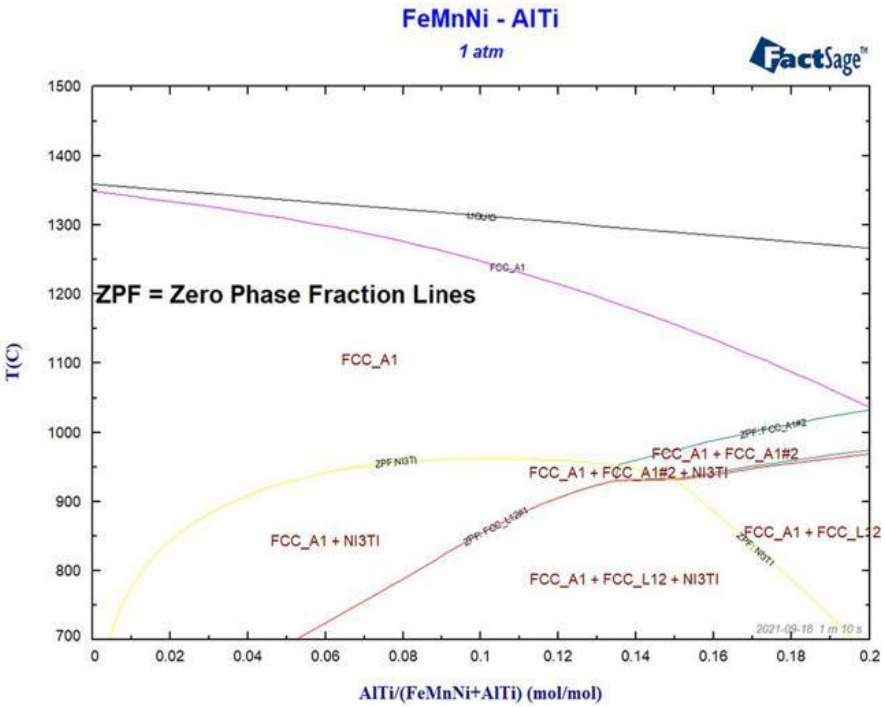

Figure 10: FactStage phase predictions for the pseudobinary FeMnNi–AlTi phase diagram, showing FCC_A1 (first FCC solid solution), FCC_A1#2 (second FCC solid solution), Ni3Ti intermetallic phase, L12 phase

Table 5 The calculated element compositions from various EDS point scans, for the Fe-rich matrices in the as-cast (A.C.), solution-treated (S.T.) and 160 h aged specimen

	Al	Ti	Fe	Mn	Ni	Al/Ti
A.C.	6.0 ± 0.26	5.7 ± 0.2	**38.8** ± 0.6	23.4 ± 0.7	26. ± 0.1	0.51
S.T.	5.2 ± 0.05	7.9 ± 0.01	**40.7** ± 0.15	15.9 ± 0.3	30.6 ± 0.2	0.41
160 h	3.9 ± 0.3	3.3 ± 0.3	**46.0** ± 0.8	19.1 ± 0.9	27.6 ± 1.2	0.54

The Fe content (bold) does verify the enrichment in Fe in this rich in Fe area

Table 6 The calculated element compositions from various EDS point scans, for the Ni-rich matrices in the as-cast (A.C.), solution-treated (S.T.) and 160 h aged specimen

	Al	Ti	Fe	Mn	Ni	Al/Ti
A.C.	9.4 ± 1.4	12.1 ± 2.7	22.9 ± 3.1	21.4 ± 0.6	**34.1** ± 1.2	0.44
S.T.	12.3 ± 0.2	11.9 ± 0.2	24.4 ± 0.5	13.9 ± 0.2	**37.5** ± 0.3	0.51
160 h	15.4 ± 1.0	5.3 ± 0.5	16.9 ± 8.3	20.5 ± 0.9	**41.9** ± 5.9	**0.74**

The Ni content (bold) does verify the enrichment in Ni in this rich in Ni area. It is also evident that the Al/Ti ratio, after 160 h heat treatment is also significantly increased (bold).

Table 7 Heat of formation of the 5 candidate Heusler compounds, as collected through the available literature.

Ni_2AlFe	Ni_2AlMn	Ni_3Al	Ni_2Al_2 (NiAl)	Ni_2AlTi
−22 kJ/mol	− 22.29 kJ/mol − 32 kJ/mol	− 41 kJ/mol	**− 48.42 kJ/mol**	**− 55.8 kJ/mol−65 kJ/mol**

The lower ΔH of the Ni_2AlTi phase (bold) compared to that of NiAl (bold) also supports the stability of the Heusler Ni_2AlTi phase

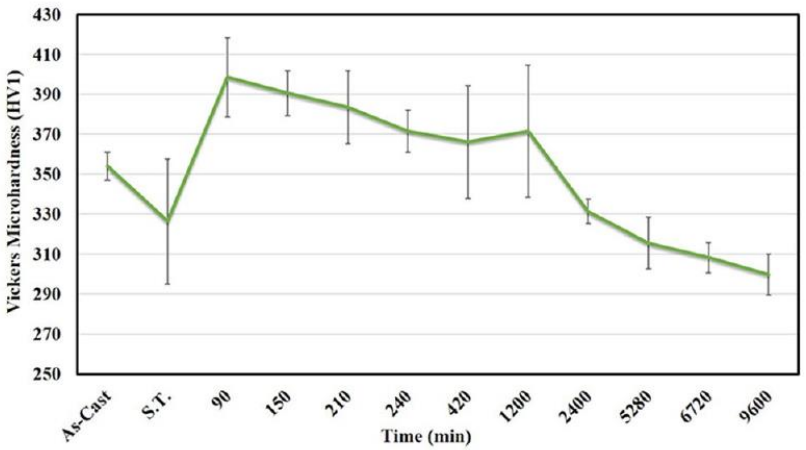

Figure 11: Vickers HV1 microhardness versus each alloy's state. The various thermal treatments seem to impact the microhardness of each alloy.

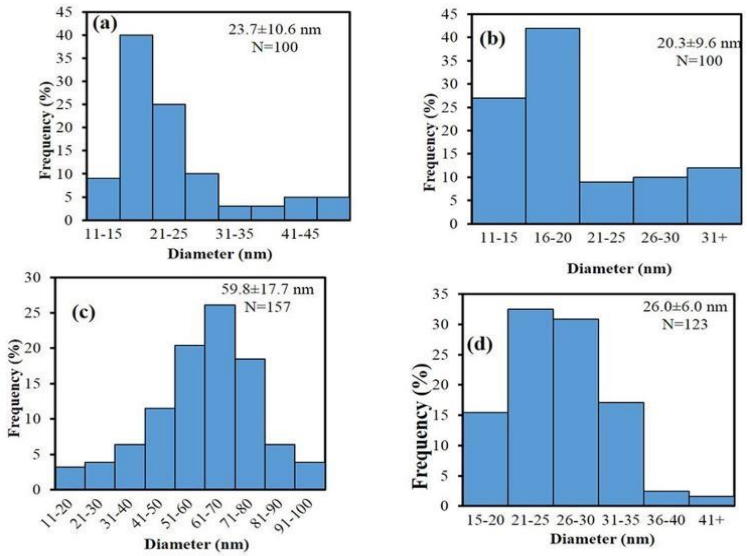

Figure 12: Diameter distribution histogram of precipitates in (a) Fe-rich region of the A.C. alloy, (b) Ni-rich region of the A.C. alloy, (c) Fe-rich region of the 160 h alloy, (d) Ni-rich region of the 160 h alloy.

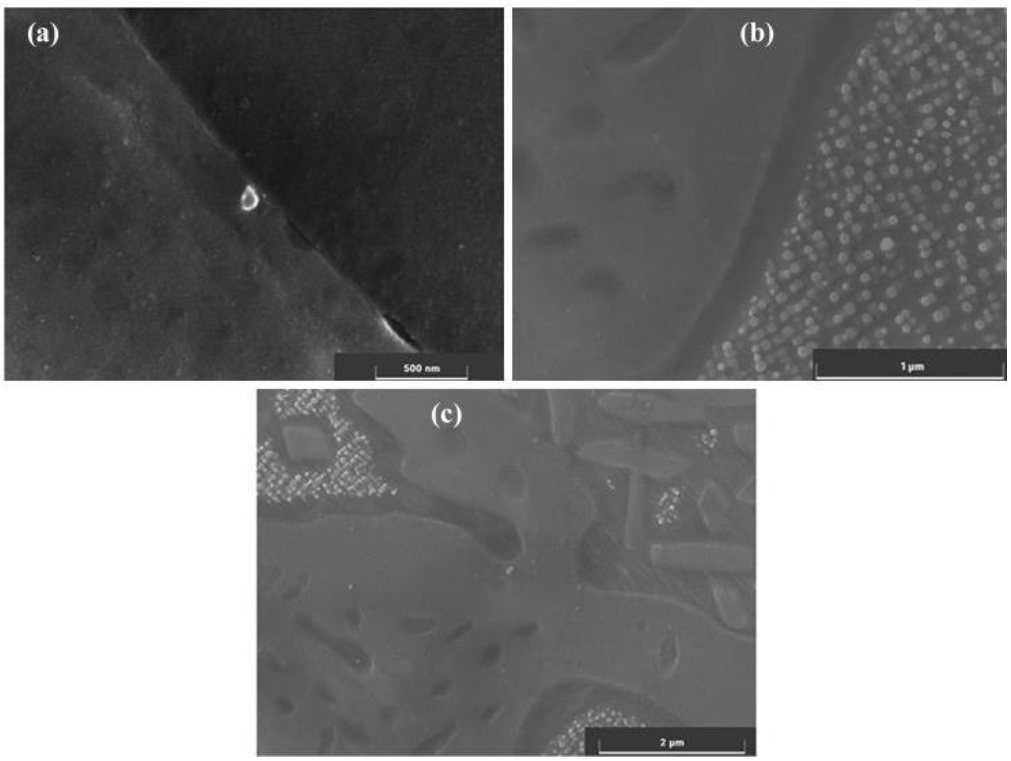

Figure 13: Secondary electrons SEM image of (a) A.C and (b, c) 160-h aged specimens of (FeMnNi)84(AlTi)16 at high magnification, showing the morphologies and distribu¬tions of the nanoparticles. In both images, the left side is the Ni-rich area and on the right side the Fe-rich area. (TESCAN S8000G).

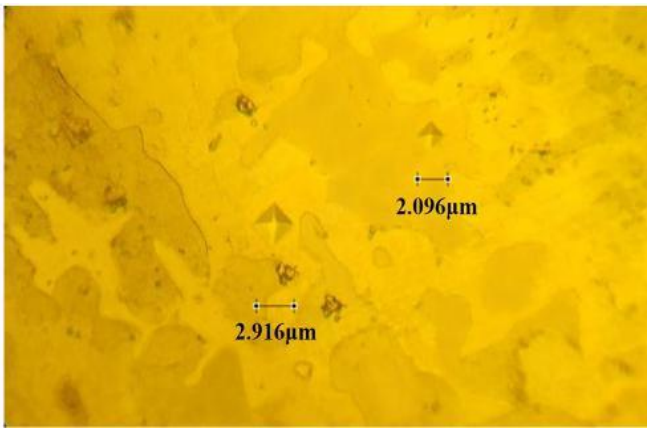

Figure 14: Vickers microhardness (HV 0,0025) indent's marks. The left mark is inside a Fe-rich area, and the right mark is in a Ni-rich area.

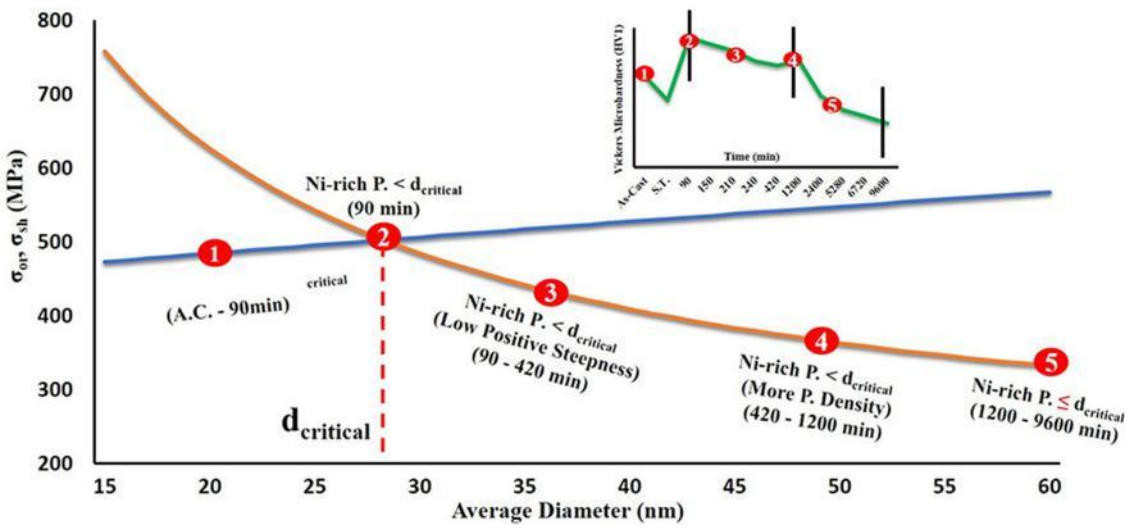

Figure 15: A theoretical schematic illustration of shearing/Orowan calculated stress versus the average diameter. The red circular marks indicate the average diameters of the hypothetical and experimental **Fe-rich** precipitation including notes with regard to the corresponding Ni-rich precipitation in each case. The diagram was schemed with the usage of equations (4), (5) and (6) and the relevant data provided in the text to simulate the present's work alloys. The last red mark was created to match the experimental area fraction and average precipitate diameter of the experimental Fe-rich 160 h microstructure

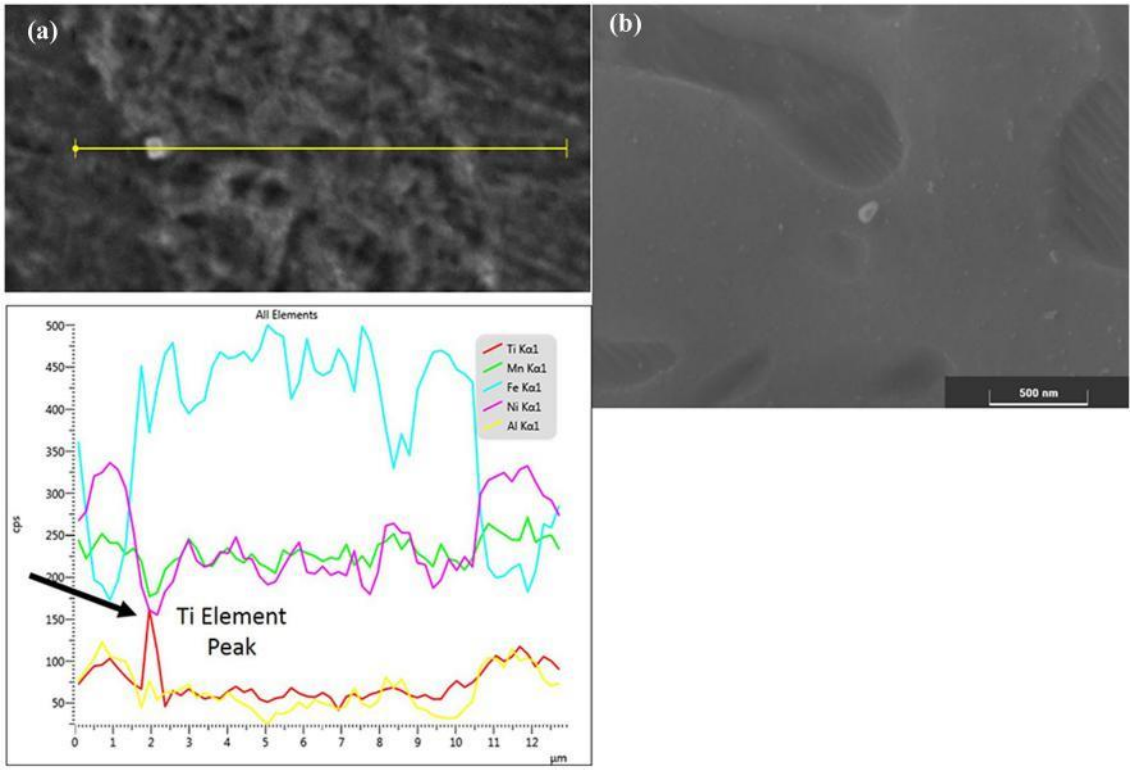

Figure 16: (**a**) EDS line scan on a bulky "island"-like precipitate, close the grain boundary on 160 h aged alloy. (JEOL 6510 LV). (**b**) High-magnification secondary electrons SEM image of an island-like precipitate in the 160 h aged specimen. (TESCAN S8000G).

References

1. B. Cantor, I.T.H. Chang, P. Knight, A.J.B. Vincent, Microstruc-tural development in equiatomic multicomponent alloys. Mater. Sci. Eng. A. **375–377**(1–2), 213–218 (2004). https://doi.org/10. 1016/j.msea.2003.10.257
2. J.W. Yeh et al., Nanostructured high-entropy alloys with multiple principal elements: Novel alloy design concepts and outcomes. Adv. Eng. Mater. **6**(5), 299–303 (2004). https://doi.org/ 10. 1002/adem. 200300567
3. Y. Zhang, *High entropy materials: A brief introduction*, 1st edn (Springer Nature Singapore Pte Ltd., Singapore, 2019) https:// doi.org/10.1007/978-981-13-8526-1
4. P. P. Murty, B.S., Yeh, J.W., Ranganathan, S., Bhattacharjee, *High-Entropy Alloys*, 2nd Edition. 2019. doi: https://doi.org/10.1016/B978-0-12-816067-1.00002-3
5. M. C. G. J. Yeh, P. K. Liaw, and Y. Zhang, *High-Entropy Alloys: Fundamentals and Applications*, 1st Edition. 2016. doi: https://doi.org/10. 1007/978-3-319-27013-5
6. R. Wang et al., Effect of lattice distortion on the diffusion behavior of high-entropy alloys. J. Alloys Compd. **825**, 154099 (2020). https://doi.org/10. 1016/j.jallcom.2020.154099
7. R.O. Ritchie, The conflicts between strength and toughness. Nat. Mater. **10**(11), 817–822 (2011). https://doi.org/10. 1038/nmat3 115
8. Z.B. Jiao, J.H. Luan, M.K. Miller, C.Y. Yu, C.T. Liu, Effects of Mn partitioning on nanoscale precipitation and mechanical properties of ferritic steels strengthened by NiAl nanoparticles. Acta Mater. **84**, 283–291 (2015). https://doi.org/10.1016/j.actam at.2014.10.065
9. W. Steurer, Single-phase high-entropy alloys – A critical update. Mater. Charact. **162**, 110179 (2020). https://doi.org/10.1016/j.matchar.2020.110179
10. Y.T. Chen, Y.J. Chang, H. Murakami, S. Gorsse, A.C. Yeh, Designing high entropy superalloys for elevated temperature application. Scr. Mater. **187**, 177–182 (2020). https://doi.org/ 10. 1016/j.scriptamat.2020.06.002
11. Z. Li, K.G. Pradeep, Y. Deng, D. Raabe, C.C. Tasan, Metastable high-entropy dual-phase alloys overcome the strength-ductility trade-off. Nature. **534**(7606), 227–230 (2016). https://doi.org/ 10.1038/nature17981
12. L. Lin et al., A multi-phase CrMnFeCoNiAl$_{0.75}$ high-entropy alloy with high strength at intermediate temperature. Interme-tallics. **120**, 106744 (2020). https://doi.org/10. 1016/j.intermet. 2020.106744
13. O.N. Senkov, G.B. Wilks, J.M. Scott, D.B. Miracle, Mechanical properties of $_{Nb25Mo25Ta25W25}$ and $V_{20}Nb_{20}Mo_{20}Ta_{20}W_{20}$ refractory high entropy alloys. Intermetallics. **19**(5), 698–706 (2011). https://doi.org/10. 1016/j.intermet.2011.01.004
14. W. Guo, W. Dmowski, J.Y. Noh, P. Rack, P.K. Liaw, T. Egami, Local atomic structure of a high-entropy alloy: An X-Ray and neutron scattering study. Metall. Mater. Trans. A Phys. Metall. Mater. Sci. **44**(5), 1994–1997 (2013). https://doi.org/10.1007/ s11661-012-1474-0
15. J. Yaacoub, W. Abuzaid, F. Brenne, H. Sehitoglu, Superelas-ticity of $(TiZrHf)_{50Ni25Co10Cu15}$ high entropy shape memory alloy. Scr. Mater. **186**, 43–47 (2020). https://doi.org/10.1016/j. scriptamat.2020.04.017
16. Y. Zhang, T. Zuo, Y. Cheng, P.K. Liaw, High-entropy alloys with high saturation magnetization, electrical resistivity, and malleability. Sci. Rep. **3**, 1–7 (2013). https://doi.org/10.1038/srep01455
17. S.P. Wang, J. Xu, TiZrNbTaMo high-entropy alloy designed for orthopedic implants: As-cast microstructure and mechanical properties. Mater. Sci. Eng. C. **73**, 80–89 (2017). https://doi.org/ 10.1016/j.msec.2016.12.057
18. P. Edalati et al., Reversible room temperature hydrogen storage in high-entropy alloy TiZrCrMnFeNi. Scr. Mater. **178**, 387–390 (2020). https://doi.org/10.1016/j.scriptamat.2019.12.009
19. N. Ishizu, J. Kitagawa, New high-entropy alloy superconductor $Hf_{21}Nb_{25}Ti_{15}V_{15}Zr_{24}$. Results Phys. **13**(April), 102275 (2019). https://doi.org/10.1016/j.rinp.2019.102275
20. D. Li et al., Acta Materialia High-entropy $Al_{0.3}$CoCrFeNi alloy fibers with high tensile strength and ductility at ambient and cryogenic temperatures. Acta Mater. **123**, 285–294 (2017). https://doi. org/10.1016/j.actamat.2016.10.038
21. C.B. Aksoy, D. Canadinc, M.B. Yagci, Assessment of Ni ion release from TiTaHfNbZr high entropy alloy coated NiTi shape memory substrates in artificial saliva and gastric fluid. Mater. Chem. Phys. **236**(April), 121802 (2019). https://doi.org/10.1016/j. matchemphys.2019.121802
22. V. Braic, M. Balaceanu, M. Braic, A. Vladescu, S. Panseri, A. Russo, Characterization of multi-principal-element (TiZrNbHfTa) N and (TiZrNbHfTa)C coatings for biomedical applications. J. Mech. Behav. Biomed. Mater. **10**, 197–205 (2012). https://doi.org/10.1016/j.jmbbm.2012.02.020
23. T. Yang, Y. Zhao, W. Liu, J. Kai, C. Liu, $L1_2$ -strengthened high-entropy alloys for advanced structural applications. J. Mater. Res. **33**, 32–41 (2018). https://doi.org/10.1557/jmr.2018.186
24. E.S. Huron et al., *Superalloys 2012* (Wiley, New York, 2012) https://doi.org/10.7449/2012/Superalloys_2012_179_188.pdf
25. T. Tsao et al., The high temperature tensile and creep behaviors of high entropy superalloy. Sci. Rep. **7**(June), 1–9 (2017). https://doi.org/10.1038/s41598-017-13026-7
26. C.M. Kuo, C.W. Tsai, Effect of cellular structure on the mechanical property of $_{Al0.2Co1.5CrFeNi1.5Ti0.3}$ high-entropy alloy. Mater. Chem. Phys. **210**, 103–110 (2018). https://doi.org/10.1016/j.match emphys.2017.10.064
27. Y. Zheng, N. Jia, F. Qian, J. Wang, Y. Xue, K. Jin, Thermal stability of $(CoCrFeNi_{)94Ti2Al4}$ alloy containing coherent nanoprecipi-tates at intermediate temperatures. Materialia. **12**, 100775 (2020). https://doi.org/10.1016/j.mtla.2020.100775
28. H. Peng, L. Hu, L. Li, W. Zhang, Ripening of $L1_2$ nano-particles and their effects on mechanical properties of $Ni_{28}Co_{28}Fe_{21}Cr_{15}Al_4Ti_4$ high-entropy alloys. Mater. Sci. Eng. A. **772**(September 2019), 138803 (2020). https://doi.org/10.1016/j. msea.2019.138803
29. S. Adil et al., On the effect of Fe in $L1_2$ strengthened Al–Co– Cr–Fe–Ni–Ti complex concentrated alloy. Materialia. **14**, 100909 (2020). https://doi.org/10.1016/j.mtla.2020.100909
30. H. Peng, L. Hu, L. Li, J. Gao, Q. Zhang, On the correlation between $L1_2$ nanoparticles and mechanical properties of $(NiCo)_{52+2x}(AlTi)_{4+2x}Fe_{29-4x}Cr_{15}$ (x=0-4) high-entropy alloys. J. Alloys Compd. (2020). https://doi.org/10.1016/j.jallcom.2019.152750
31. V. Nandal et al., Enhanced age hardening effects in FCC based $Co_{1.5}CrFeNi_{1.5}$ high entropy alloys with varying Ti and Al contents. Materialia. **13**(July), 100823 (2020). https://doi.org/10. 1016/j.mtla.2020.100823
32. P. Bała, K. Górecki, W. Bednarczyk, M. Watroba, S. Lech, J. Kawałko, Effect of high-temperature exposure on the microstructure and mechanical properties of the $Al_5Ti_5Co_{35}Ni_{35}Fe_{20}$ high-entropy alloy. J. Mater. Res. Technol. **9**(1), 551–559 (2020). https://doi.org/10.1016/j.jmrt.2019.10.084
33. T. Yang et al., Control of nanoscale precipitation and elimination of intermediate-temperature embrittlement in multicomponent high-entropy alloys. Acta Mater. **189**, 47–59 (2020). https://doi. org/10.1016/j.actamat.2020.02.059

34. D. Chen et al., Synergistic effect of Ti and Al on $L1_2$-phase design in CoCrFeNi-based high entropy alloys. Intermetallics. **110**(April), 106476 (2019). https://doi.org/10. 1016/j.intermet. 2019.106476
35. Y.Y. Zhao, H.W. Chen, Z.P. Lu, T.G. Nieh, Thermal stability and coarsening of coherent particles in a precipitation-hardened $(NiCoFeCr)_{94}Ti_2Al_4$ high-entropy alloy. Acta Mater. **147**, 184–194 (2018). https://doi.org/10.1016/j.actamat.2018.01.049
36. K. Ming, X. Bi, J. Wang, Realizing strength-ductility combination of coarse-grained $Al_{0.2}Co_{1.5}CrFeNi_{1.5}Ti_{0.3}$ alloy via nano-sized, coherent precipitates. Int. J. Plast. **100**, 177–191 (2018). https:// doi.org/10.1016/j.ijplas.2017.10.005
37. T. Yang et al., Multicomponent intermetallic nanoparticles and superb mechanical behaviors of complex alloys. Science (80-). **362**(6417), 933–937 (2018). https://doi.org/10.1126/science.aas8815
38. Y.L. Zhao et al., Heterogeneous precipitation behavior and stacking-fault-mediated deformation in a CoCrNi-based medium-entropy alloy. Acta Mater. **138**, 72–82 (2017). https://doi.org/10. 1016/j.actamat.2017.07.029
39. Z. Wang, A. Genc, I. Baker, Direct versus indirect particle strengthening in a strong, ductile FeNiMnAlTi high entropy alloy. Mater. Charact. **132**(August), 156–161 (2017). https://doi.org/10. 1016/j.matchar.2017.08.019
40. J.Y. He et al., Precipitation behavior and its effects on tensile properties of FeCoNiCr high-entropy alloys. Intermetallics. **79**, 41–52 (2016). https://doi.org/10.1016/j.intermet.2016.09.005
41. J.Y. He et al., A precipitation-hardened high-entropy alloy with outstanding tensile properties. Acta Mater. **102**, 187–196 (2016). https://doi.org/10.1016/j.actamat.2015.08.076
42. H.M. Daoud, A.M. Manzoni, N. Wanderka, U. Glatzel, High-temperature tensile strength of $Al_{10}Co_{25}Cr_8Fe_{15}Ni_{36}Ti_6$ compositionally complex alloy (high-entropy alloy). Jom. **67**(10), 2271–2277 (2015). https://doi.org/10.1007/s11837-015-1484-7
43. C.W. Lin, M.H. Tsai, C.W. Tsai, J.W. Yeh, S.K. Chen, Microstructure and aging behaviour of $Al_5Cr_{32}Fe_{35}Ni_{22}Ti_6$ high entropy alloy. Mater. Sci. Technol. (United Kingdom). **31**(10), 1165–1170 (2015). https://doi.org/10.1179/1743284715Y.0000000025
44. Y. Qi, Y. Wu, T. Cao, L. He, F. Jiang, J. Sun, $L2_1$-strengthened face-centered cubic high-entropy alloy with high strength and ductility. Mater. Sci. Eng. A. **797**, 140056 (2020). https://doi.org/10. 1016/j.msea.2020.140056
45. Y.T. Chen et al., Hierarchical microstructure strengthening in a single crystal high entropy superalloy. Sci. Rep. **10**(1), 1–12 (2020). https://doi.org/10.1038/s41598-020-69257-8
46. S. Gorsse, Y.T. Chen, W.C. Hsu, H. Murakami, A.C. Yeh, Modeling the precipitation processes and the formation of hierarchical microstructures in a single crystal high entropy superalloy. Scr. Mater. **193**, 147–152 (2021). https://doi.org/10.1016/j.scriptamat. 2020.11.002
47. S. Dasari et al., Discontinuous precipitation leading to nano-rod intermetallic precipitates in an $Al_{0.2}Ti_{0.3}Co_{1.5}CrFeNi_{1.5}$ high entropy alloy results in an excellent strength-ductility combination. Mater. Sci. Eng. A. (2020). https://doi.org/10.1016/j.msea. 2020.140551
48. R.C. Reed, The superalloys: fundamentals and applications. Cambridge University Press. (2016). https://doi.org/10.1017/CBO9780511541285.004
49. T. Rieger, J. Joubert, L. Perrière, I. Guillot, J. Couzinié, Materialia Study of the FCC + $L1_2$ two-phase region in complex concentrated alloys based on the Al–Co–Cr–Fe–Ni–Ti system. Materialia. **14**, 100905 (2020). https://doi.org/10.1016/j.mtla.2020.100905
50. S. Jiang et al., Ultrastrong steel via minimal lattice misfit and high-density nanoprecipitation. Nature. **544**(7651), 460–464 (2017). https://doi.org/10.1038/nature22032
51. R.C. Reed, C.M.F. Rae, *Physical Metallurgy of the Nickel- Based Superalloys* (Elsevier, Amsterdam, 2014), p. 2215. https://doi.org/10.1016/B978-0-444-53770-6.00022-8
52. R. Singh, *Applied Welding Engineering: Processes, Codes, and Standarts*, 3rd Edition, Butterworth-Heinemann, 2020. doi: https://doi.org/10.1016/B978-0-12-821348-3.00001-X.
53. S. Guo, C.T. Liu, Phase stability in high entropy alloys: formation of solid-solution phase or amorphous phase. Prog. Nat. Sci. Mater. Int. **21**(6), 433–446 (2011). https://doi.org/10.1016/S1002-0071(12) 60080-X
54. Y. Zhang, Y.J. Zhou, J.P. Lin, G.L. Chen, P.K. Liaw, Solid solution phase formation rules for multi-component alloys. Adv. Eng. Mater. **10**, 534–538 (2008)
55. Z. Wang, Y. Huang, Y. Yang, J. Wang, C.T. Liu, Atomic-size effect and solid solubility of multicomponent alloys. Scr. Mater. **94**, 28–31 (2015). https://doi.org/10.1016/j.scriptamat.2014.09.010
56. M.C. Troparevsky, J.R. Morris, P.R.C. Kent, A.R. Lupini, G.M. Stocks, Criteria for predicting the formation of single-phase high-entropy alloys. Phys. Rev. X. **5**(1), 1–6 (2015). https://doi.org/10. 1103/PhysRevX.5.011041
57. D.J.M. King, S.C. Middleburgh, A.G. McGregor, M.B. Cortie, Predicting the formation and stability of single phase high-entropy alloys. Acta Mater. **104**, 172–179 (2016). https://doi.org/10.1016/j. actamat.2015.11.040
58. S. Guo, C. Ng, J. Lu, C.T. Liu, Effect of valence electron concentration on stability of fcc or bcc phase in high entropy alloys. J. Appl. Phys. (2011). https://doi.org/10.1063/1.3587228
59. S. Guo, Q. Hu, C. Ng, C.T. Liu, More than entropy in high entropy alloys: forming solid solutions or amorphous phase. Intermetallics. **41**, 96–103 (2013)
60. X. Yang, Y. Zhang, Prediction of high-entropy stabilized solid-solution in multi-component alloys. Mater. Chem. Phys. **132**(2–3), 233–238 (2012). https://doi.org/10.1016/j.matchemphys.2011.11. 021
61. O.N. Senkov, D.B. Miracle, A new thermodynamic parameter to predict formation of solid solution or intermetallic phases in high entropy alloys. J. Alloys Compd. **658**, 603–607 (2016). https://doi. org/10.1016/j.jallcom.2015.10.279
62. X. Jin, Y. Zhou, L. Zhang, X. Du, B. Li, A new pseudo binary strategy to design eutectic high entropy alloys using mixing enthalpy and valence electron concentration. Mater. Des. **143**, 49–55 (2018). https://doi.org/10.1016/j.matdes.2018.01.057
63. B.S. Murty, J.W. Yeh, R. Ranganathan, *High-entropy Alloys*, 1st edn (Butterworth-Heinemann, London, 2014)
64. D. Batalu, G. Coşmeleaţă, A. Aloman, Critical analysis of the Ti-Al phase diagrams. UPB Sci. Bull. Ser. B Chem. Mater. Sci. **68**(4), 77–90 (2006)
65. D. Batalu, H. Guoqiu, A. Aloman, and G. Coşmeleaţă, "A review on TiNi shape memory alloys (SMA) used for medical applications . Recycling aspects," no. November, pp. 1–10, 2000.
66. R.F. Zhang, B.X. Liu, Proposed model for calculating the standard formation enthalpy of binary transition-metal systems. Appl. Phys. Lett. **81**(7), 1219–1221 (2002). https://doi.org/10.1063/1.1499510
67. R.F. Zhang, K. Rajan, Statistically based assessment of formation enthalpy for intermetallic compounds. Chem. Phys. Lett. **612**, 177– 181 (2014). https://doi.org/10.1016/j.cplett.2014.08.024
68. R.F. Zhang, S.H. Sheng, B.X. Liu, Predicting the formation enthalpies of binary intermetallic compounds. Chem. Phys. Lett. **442**(4–6), 511–514 (2007). https://doi.org/10.1016/j.cplett.2007.06.031

69. L. Zhang et al., Phase equilibria and thermal analysis in the Fe-Mn-Ni system. Int. J. Mater. Res. **100**(2), 160–175 (2009). https://doi.org/10.3139/146.110002
70. X. Chen et al., Influences of Ti additions on the microstructure and tensile properties of $AlCoCrFeNi_{2.1}$ eutectic high entropy alloy. Intermetallics. **128**, 107024 (2021). https://doi.org/10.1016/j.inter met.2020.107024
71. J. Jung, G. Ghosh, D. Isheim, G.B. Olson, Precipitation of Heusler phase (Ni_2TiAl) from B2-TiNi in Ni-Ti-Al and Ni-Ti-Al-X (X = Hf, Zr) alloys. Metall. Mater. Trans. A Phys. Metall. Mater. Sci. **34**(6), 1221–1235 (2003). https://doi.org/10.1007/s11661-003-0233-7
72. J. Nakata et al., Thermal conductivity in X_2YZ Heusler type inter-metallic compounds. Mater. Trans., JIM. **37**, 442–447 (1996)
73. D. Choudhuri et al., Formation of a Huesler-like $L2_1$ phase in a CoCrCuFeNiAlTi high-entropy alloy. Scr. Mater. **100**, 36–39 (2015). https://doi.org/10.1016/j.scriptamat.2014.12.006
74. T. Yang et al., Nanoparticles-strengthened high-entropy alloys for cryogenic applications showing an exceptional strength-ductility synergy. Scr. Mater. **164**, 30–35 (2019). https://doi.org/10.1016/j. scriptamat.2019.01.034
75. E.P. George, W.A. Curtin, C.C. Tasan, High entropy alloys: A focused review of mechanical properties and deformation mechanisms. Acta Mater. **188**, 435–474 (2020). https://doi.org/10.1016/j. actamat.2019.12.015
76. Z. Li, S. Zhao, R.O. Ritchie, M.A. Meyers, Mechanical properties of high-entropy alloys with emphasis on face-centered cubic alloys. Prog. Mater. Sci. **102**, 296–345 (2019). https://doi.org/10.1016/j. pmatsci.2018.12.003
77. S. Gorsse, M.H. Nguyen, O.N. Senkov, D.B. Miracle, Database on the mechanical properties of high entropy alloys and complex concentrated alloys. Data Br. **21**, 2664–2678 (2018). https://doi.org/10. 1016/j.dib.2018.11.111
78. L. Hu, H. Peng, I. Baker, L. Li, W. Zhang, T. Ngai, Characterization of high-strength high-nitrogen austenitic stainless steel synthesized from nitrided powders by spark plasma sintering. Mater. Charact. **152**, 76–84 (2019). https://doi.org/10.1016/j.matchar.2019.04.005
79. F. Meng, I. Baker, Nitriding of a high entropy FeNiMnAlCr alloy. J. Alloys Compd. **645**, 376–381 (2015). https://doi.org/10.1016/j.jallcom.2015.05.021
80. E.J. Pavlina, C.J. Van Tyne, Correlation of Yield strength and Tensile strength with hardness for steels. J. Mater. Eng. Perform. **17**(6), 888–893 (2008). https://doi.org/10.1007/s11665-008-9225-5
81. W. Soboyejo, *Mechanical Properties of Engineered Materials*, 1st edn (CRC Press, Boca Raton, 2002) https://doi.org/10.1201/97802 03910399
82. V. Leskovsek, M. Kalin, J. Vizintin, Influence of deep-cryogenic treatment on wear resistance of vacuum heat-treated HSS. Vacuum. **80**, 507–518 (2006). https://doi.org/10.1016/j.vacuum.2005.08.023
83. H.A. Murdoch, C.A. Schuh, Estimation of grain boundary segregation enthalpy and its role in stable nanocrystalline alloy design. J. Mater. Res. **28**(16), 2154–2163 (2013). https://doi.org/10.1557/jmr. 2013.211
84. Z.B. Jiao, J.H. Luan, M.K. Miller, C.Y. Yu, Y. Liu, C.T. Liu, Precipitate transformation from NiAl-type to Ni_2AlMn-type and its influence on the mechanical properties of high-strength steels. Acta Mater. **110**, 31–43 (2016). https://doi.org/10.1016/j.actamat.2016. 03.024
85. M. Yin, P. Nash, W. Chen, S. Chen, Standard enthalpies of formation of selected Ni_2YZ Heusler compounds. J. Alloys Compd. **660**, 258–265 (2016). https://doi.org/10.1016/j.jallcom.2015.11.126
86. T. Zhang, D. Wang, J. Zhu, H. Xiao, C.T. Liu, Y. Wang, Non-conventional transformation pathways and ultrafine lamellar structures in γ-TiAl alloys. Acta Mater. **189**, 25–34 (2020). https://doi.org/10. 1016/j.actamat.2020.02.053
87. A. Boyne et al., Pseudospinodal mechanism for fine α/β microstructures in β-Ti alloys. Acta Mater. **64**, 188–197 (2014). https://doi.org/10.1016/j.actamat.2013.10.026

https://dspace.org/

(FeMnNi)84(AlTi)16 highentropy alloy: correlation of microstructure, strengthening mechanisms and hardness at various conditions (AsCast, solution treated, aged)

Konakoglou, Kimon; Mathiou, C.; Georgatis, E.; Georgarakis, Konstantinos; Karantzalis, A. E.

2022-04-01
Springer
https://doi.org/10.1007/s13632-022-00846-x
Konakoglou K, Mathiou C, Georgatis E, et al., (2022) (FeMnNi)84(AlTi)16 highentropy alloy: correlation of microstructure, strengthening mechanisms and hardness at various conditions (AsCast, solution treated, aged), Metallography, Microstructure, and Analysis, Volume 11, April 2022, pp. 309-326

Downloaded from a DSpace repository. https://dspace.org/